

Communication

Ferroelectric Polarization in an h-BN-Encapsulated 30°-Twisted Bilayer–Graphene Heterostructure

Lingling Ren^{1,2} and Baojuan Dong^{1,2,*} 

¹ State Key Laboratory of Quantum Optics and Quantum Optics Devices, Institute of Opto-Electronics, Shanxi University, Taiyuan 030006, China

² Collaborative Innovation Center of Extreme Optics, Shanxi University, Taiyuan 030006, China

* Correspondence: dongbaojuan.1989@gmail.com

Abstract: Recently, the emergent two-dimensional (2D) ferroelectric materials have provided new possibilities for the miniaturization of ferroelectric systems and the integration of novel 2D nano-electronic devices. In addition to the intrinsic ferroelectrics exfoliated from bulk, 2D heterostructures hybridized from electrically non-polarized van der Waals (vdW) materials have also been proven to be a promising platform for the construction of ferroelectricity. Here, we report 30° twisted bilayer–graphene (TBLG) incommensurate moiré superlattice encapsulated by hexagonal boron nitride (h-BN), in which robust hysteretic resistance was detected at the top interface between h-BN and the TBLG from room temperature down to 40 mK. The hysteretic phenomenon can be understood by the extra carrier induced by the interfacial 2D ferroelectric polarization, which is estimated to be around 0.7 pC/m. Our work of interfacial ferroelectric heterostructure achieved by a TBLG/h-BN hybrid system expands the 2D ferroelectric families and opens more possibilities for future coupling the ferroelectricity with rich electronic and optical properties in vdW twistrionic devices.

Keywords: incommensurate twisted bilayer–graphene; interface ferroelectric polarization; electronic hysteresis



Citation: Ren, L.; Dong, B. Ferroelectric Polarization in an h-BN-Encapsulated 30°-Twisted Bilayer–Graphene Heterostructure. *Magnetochemistry* **2023**, *9*, 116. <https://doi.org/10.3390/magnetochemistry9050116>

Academic Editors: Boris Tsukerblat and Carlos J. Gómez García

Received: 28 February 2023

Revised: 17 April 2023

Accepted: 25 April 2023

Published: 26 April 2023



Copyright: © 2023 by the authors. Licensee MDPI, Basel, Switzerland. This article is an open access article distributed under the terms and conditions of the Creative Commons Attribution (CC BY) license (<https://creativecommons.org/licenses/by/4.0/>).

1. Introduction

Ferroelectric materials possess switchable spontaneous long-range electrical polarization, which holds great promise to be essential components of nonvolatile random-access memory devices, ferroelectric field-effect transistors, and emerging conceptual logics [1–4]. The pioneer investigations on two-dimensional (2D) van der Waals (vdW) ferroelectric materials have brought new possibilities in this field [5]. The 2D vdW ferroelectric materials, which are either chemical vapor deposited or mechanically exfoliated down to the atomic layer limit, can be further stacked freely together with other 2D functional materials without the constraint of lattice match. To date, exfoliated monolayer ferroelectrics with vertical polarization have been experimentally confirmed in aIn_2Se_3 and CuInP_3S_6 , while 2D ferroelectric materials with in-plane polarization are also reported in SnTe , bIn_2Se_3 , and SnS [6–15]. In addition to the intrinsic ferroelectric polarization, vdW heterostructures consisting of non-polarized building blocks such as h-BN/bilayer-graphene/h-BN systems [16–20] have become a cutting-edge topic due to the interfacial ferroelectric polarization, known as 2D sliding-ferroelectricity.

Unique to 2D materials, the twisted angle is another essential degree of freedom, which largely influences the physical properties of the host system [21–25]. The interaction-induced unconventional superconductivity, correlated insulator, orbital ferromagnetism, and topological phenomena such as quantum anomalous hall effect have been reported in the twisted-graphene devices. Surprisingly, the h-BN-encapsulated magic-angle TBLG was recently reported to concomitantly hold interfacial ferroelectricity together with superconductivity, which yields an electrically switchable bistable superconductor [26]. The

electron-correlation strength has a close relationship with the twist angle in the TBLG system. For example, the $\sim 1.1^\circ$ twisted bilayer-graphene exhibits a flat band at the Fermi level and endevors the strongest intra- and inter-layer interactions, while the weakest interlayer interaction lies in an incommensurate state with a twist angle of 30° [27–30]. Up to now, the interfacial ferroelectrics were mostly reported in the strong coupling regime, such as aligned h-BN/Bernal stacking bilayer-graphene and h-BN/ 1.1° TBLG system, while studies on interface polarization between h-BN and weak coupling twisted bilayer-graphene is missing.

In the work, we fabricated high-quality h-BN-encapsulated bilayer-graphene twisted at 30° with weak interlayer coupling. The device was fabricated and patterned into hall bar geometry. Electronic properties were characterized using the standard four-probe method. While the back gate sweeping shows field effect curves without hysteresis, top gate sweeping exhibits clear hysteretic behavior from room temperature down to a base temperature of 4 mK. The top gate hysteresis is attributed to a typical process of 2D interfacial ferroelectric polarization, estimated to be 0.7 pC/m. Among the seven samples measured in our study, only one sample was found to show such ferroelectricity. Our findings of the interfacial ferroelectric polarization in the h-BN-encapsulated incommensurate twisted bilayer-graphene expand the 2D ferroelectric families and provides a new platform to further coupling other quantum degrees of freedom to the ferroelectricity in the twisted moiré system.

2. Methods

To fabricate the devices needed for this study, the selected uniform h-BN with a thickness of about 27 nm (Figure 1c) was first picked up by a polydimethylsiloxane (PDMS)/polypropylene carbonate (PPC) stamp at about 42°C . Secondly, van der Waals electrical adsorption force between the h-BN and graphene helped us to pick up one-half of the cut graphene, which was achieved by covering the h-BN on PDMS/PPC/h-BN stamp on the graphene. After picking up the first half graphene, the stamp was held still, and then we rotated the substrate with another half of the cut graphene at about 30° . After that, the picking-up step was applied again for the left half graphene. As shown in Supplementary Figure S1, sample S1 was fabricated using an h-BN as the picking-up flake. Additionally, the TBLG was obtained by first cutting the MLG into two pieces, followed by two consecutive picking-up steps (yellow first, and then green, highlighted in Supplementary Figure S1b) with a rotation angle of 30° . It is seen that, in Supplementary Figure S1c, the h-BN crystalline axis does not seem to be 30° aligned to either of the graphene flakes, which may be different from the ferroelectricity arising from 30° aligned h-BN/graphene [20]. Up to now, the stack with h-BN/twisted graphene was well prepared. Thirdly, the back gate was fabricated by transferring the screened h-BN (about 40 nm shown in Figure 1c) onto the 5 mm width metal gate Ti (5 nm)/Au (30 nm), which was fabricated on Silicon/Silicon dioxide 300 nm substrate under the treatment of standard electron beam lithography (EBL) and electron beam evaporation (EB). Subsequently, the h-BN/twisted graphene stack was transferred onto the back gate, forming the h-BN-encapsulated twisted graphene device. Then the EBL and reactive ion etching (RIE) were used to pattern the hall bar geometry for the key section of the device. Ti (5 nm)/Au (50 nm) one-dimensional edge contacts were made by using the EBL, RIE, and EB techniques. After depositing 30 nm AlO_x by atomic layer deposition, a large top gate with Ti (5 nm)/Au (30 nm), which covered the whole hall bar region, was fabricated on top of AlO_x dielectric layer.

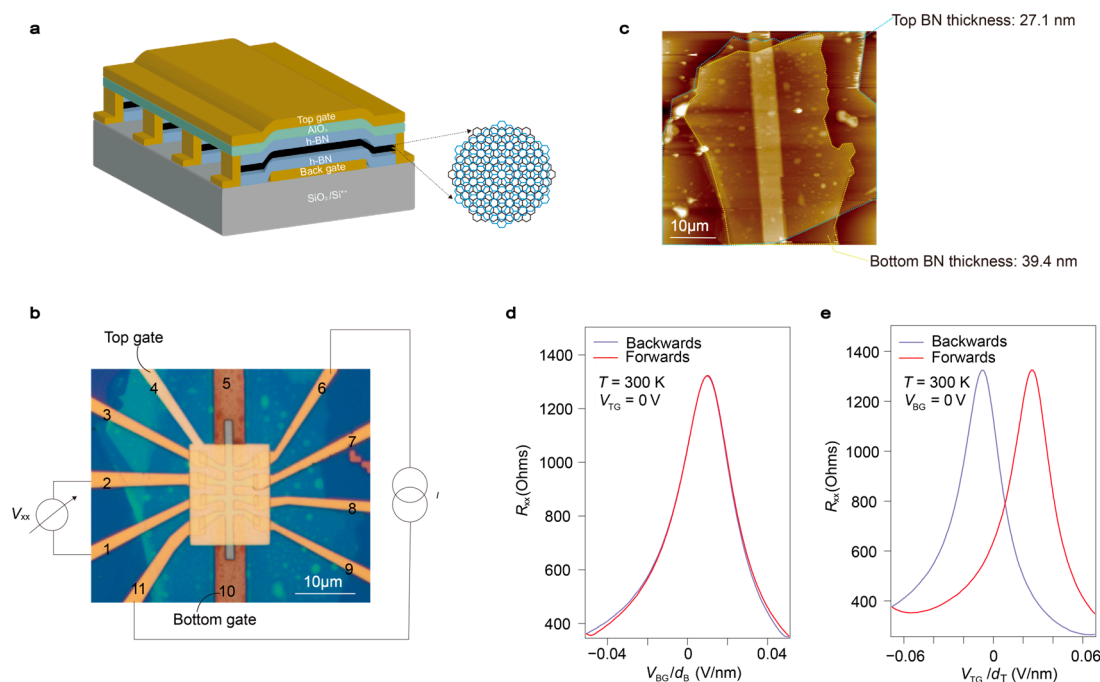


Figure 1. Device structure and characterization. (a) Schematic diagram of a dual gate patterned twisted graphene device. The twisted graphene (black block), where the twisted detail between the two layers is shown by the side, is encapsulated by the two 30–40 nm h-BN, and the device is patterned as a Hall bar structure. The top and back gates are gold electrodes, which are separated by the h-BN and AlO_x and h-BN, respectively. (b) The optical image of the device. (c) The atomic force microscope of the un-patterned h-BN-encapsulated twisted graphene stack, where the outline of the top (27.1 nm) and bottom h-BN (39.4 nm) are plotted by blue and yellow dotted lines. (d,e) The room temperature four-probe resistance of twisted graphene as a function of the back gate and top gate in the backward (blue) and upwards (red) scan directions are shown in d and e, respectively. The standard four-terminal resistance measurement is taken to avoid the impact of contact resistance.

The electronic transport properties were characterized by using the standard four-probes technique. A 500 nA alternating current I_{ac} was supplied to the source of the device, as shown in Figure 1b. Then, longitudinal voltage V_{xx} was detected by a Phase-locked amplifier SR830 with a frequency locked in 177.77 HZ. The thickness of top and bottom h-BN was characterized to be 27.1 nm and 39.4 nm by using AFM, which were outlined in blue and yellow dotted lines in Figure 1c, respectively.

3. Results and Discussion

The h-BN-encapsulated TBLG device was fabricated using the dry transfer technique [31,32]. Bulk crystal graphite and h-BN were firstly exfoliated and then transferred onto SiO₂/Si⁺⁺ substrates. Monolayer graphene and few-layered h-BN were identified by the contrast in the optical microscope combing with the surface morphology and thickness check in the atomic force microscope (AFM). Then the selected monolayer graphene flakes were cut into two pieces using the anodic oxidation nanolithography mode of AFM to have identical crystallographic orientation for further stacking of TBLG [33,34]. Four probes of the low-frequency ac lock-in technique were used to characterize the electronic transport properties of the as-prepared devices. Details of the heterostructure and device fabrication can be found in the Section 2.

Schematics and optical images of a typical dual-gated h-BN-encapsulated TBLG device are shown in Figure 1a,b, respectively. The dual gate configuration allows us to independently tune the carrier density, n , and the out-of-plane electric displacement field, D , in TBLG, respectively. Room temperature field effect curves as a function of the top and

bottom gate, with the other gate grounded during measuring, are shown in Figure 1d,e, respectively. The x -axes, i.e., the gate voltages, are renormalized by the distance between the gate and the TBLG channel. While the back gate sweep shows negligible hysteresis in the trace and retrace curves, the top gate sweep however exhibits a substantial hysteretic behavior, as shown in Figure 1e.

Transport properties were carefully characterized in a dilution refrigerator down to a temperature of $T = 40$ mK. R_{XX} as a function of dual gate sweeping was measured, where the range of V_{BG} (V_{TG}) was set to be ± 12 V (± 16 V). During the scan of dual-gate mapping, the V_{TG} was set to be the fast axis, while the back gate V_{BG} was set to be the slow axis (i.e., V_{BG} is set to the next step only when the V_{TG} sweep is finished in the mapping process). Only one direction of back gate scanning is shown due to its non-hysteretic characteristic. The resistance under the forward (from -16 V to 16 V) and backward (from 16 V to -16 V) scan directions of the top gate were shown in Figure 2a,b, respectively.

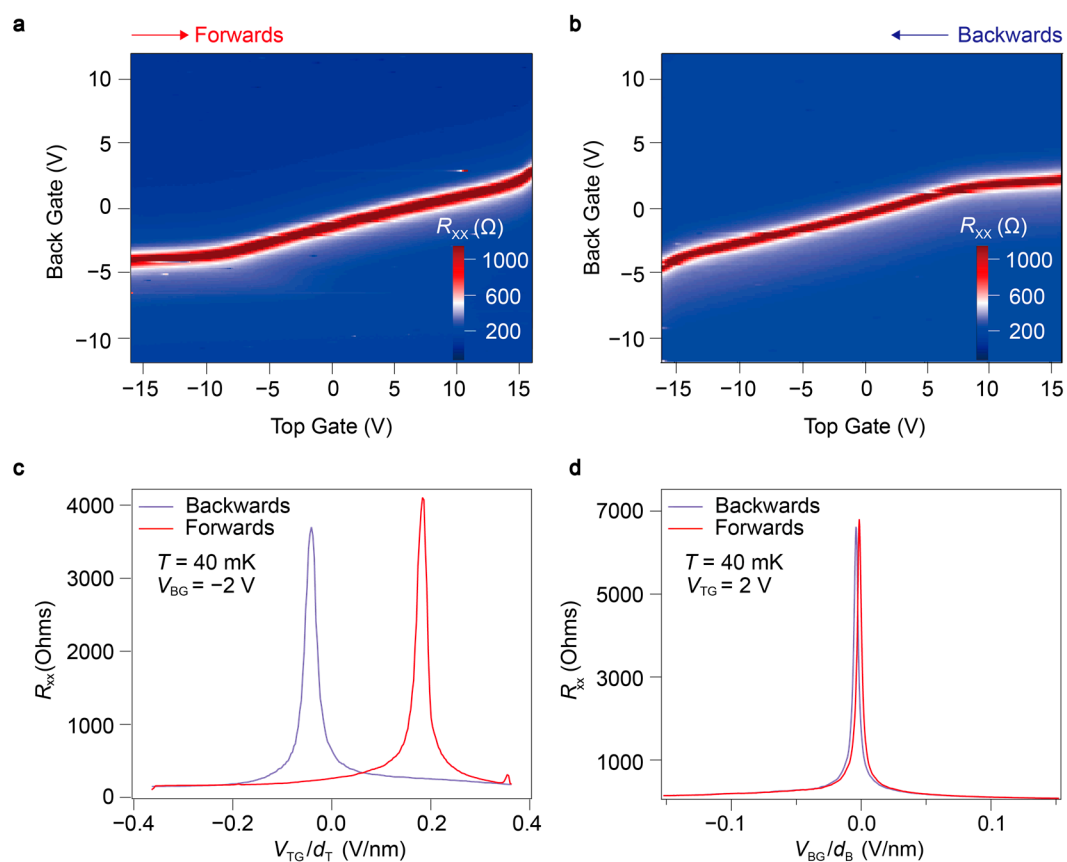


Figure 2. The low-temperature electronic properties characterization. (a,b) Dual-gate mapping of the four-probe longitudinal resistance at 40 mK with the forward and backward scan directions of the top gate. The resistance data were all taken in the upwards back gate scan direction. During the mapping scan process, the V_{TG} was set to be a fast axis, while the V_{BG} was set as the slow axis. (c) The hysteretic four-probe resistance measured at -2 V back gate at 40 mK as a function of V_{TG}/d_T , which is the top gate divided by the distance between twisted graphene and the top gate. (d) The normal four-probe resistance measured at 2 V top gate at 40 mK as a function of V_{BG}/d_B , which is the top gate divided by the distance between twisted graphene and the top gate. The downwards and upwards scan directions are in blue and red in (c,d).

Unlike the normal graphene dual-gate mapping, which was usually characterized by a straight diagonal slash resistance peak ridge, mapping for our dual gate h-BN-encapsulated TBLG showed a bent-line of resistance peak with inflection point for both up- and down-scanned directions. For the forward top gate scanning case in Figure 2a, the inflection

point occurred around $V_{TG} = -9$ V, where the resistance peak track showed a straight line nearly parallel to the V_{TG} axis before the top gate reached this point from -16 V. Within this region, the back gate worked normally, while the top gate acted similarly to ‘disabled’ with nearly no tunability. This situation is consistent with the phenomenon of ‘layer-specific anomalous screening’ (LSAS) reported in previous work for the h-BN-encapsulated bilayer-graphene devices [16,20]. Continue sweeping forwards over this inflection point, the top gate recovered its tunability, with the resistance peak starting to follow a ‘diagonal’ character as that found in a conventional dual-gate mapping of graphene. A similar phenomenon was also observed in the backward-sweeping scenario (Figure 2b). During sweeping from 16 V to 9 V, the top gate seemed to be screened with negligible tunability and a resistance peak red line paralleling to V_{TG} axis can be seen. Further sweeping downwards across the inflection point, the top gate tunability was reactivated. Comparing the mappings in Figure 2a,b, an abrupt contract of graphene-resistance peak trajectory can be seen, which confirms the presence of hysteretic behavior.

We then checked the transport-electronic properties under a single gate sweeping, with another fixed at a finite value, as shown in Figure 2c,d. With the top gate swept in between $+16$ V and 16 V back and forth while keeping the back gate fixed at $V_{BG} = -2$ V, an obvious hysteretic resistance peak was observed (Figure 2c), consistent with the hysteresis observed at zero back gate at room temperature in Figure 1e. When the top gate is fixed at $V_{TG} = 2$ V, the back gate was swept between $+12$ V and -12 V back and forth; negligible hysteresis was seen in the trace and retrace of field effect curves (Figure 2d).

Until now, we can conclude that the h-BN-encapsulated TBLG can exhibit robust hysteresis from low temperature up to room temperature. Additionally, the top gate played a key role in activating this hysteretic behavior, while the back gate performed as a normal carrier contributing gate. Such a hysteretic characteristic possibly originates from the spontaneous ferroelectric polarization between the TBLG and the top h-BN, which induces an out-of-plane built-in electric field. It is commonly acknowledged that the electrical dipole moment in a 2D sliding ferroelectric system comes from the locally non-centrosymmetric atomic stacking order at the interfaces. As in our system, only the top gate exhibits clear hysteretic behavior. We speculate that a non-centrosymmetric staking order has formed between the top h-BN and the TBLG, contributing to the electric dipoles. However, we regret that we cannot show a more in-depth analysis regarding this issue. Such ferroelectric polarization-induced built-in electric field works together with the applied top gate voltage on the twisted graphene as a combined effective top gate, forming the hysteretic transport characteristic, as reported previously in systems including bilayer-graphene aligned with h-BN on both sides [16] and bilayer-graphene aligned at 0° and 30° to h-BN for top and bottom surfaces, respectively [20]. Models of gate-specific ferroelectricity (GSFE) and concomitant anomalous screening ascribed to electron dynamics are well established in these systems, with the unconventional hysteretic characteristic (unlike the charge trapping induced hysteresis, the GSFE-induced hysteresis does not depend on sweeping rate) being the most pronounced feature as a result of the interfacial ferroelectricity.

To further understand the interfacial ferroelectric polarization, the resistance difference DR_{xx} between the measured values in Figure 2a,b was shown in Figure 3a, which exhibits a parallelogram shape highlighting the hysteresis behavior. Now, we can try to understand the “disabled” region (where the Dirac peak levels off as a function of the top gate) of the top gate tunability from the view of ferroelectric polarization. Taking the forward-scanning process of the top gate for example, which is represented by red color in Figure 3a, when the top gate was swept from -16 V to the inflection point -9 V, the built-in electric field induced by ferroelectric polarization cancels with the electrical field induced by top gating, leading to an effective screening of the electrostatic gating and hence a leveling off of resistance peak as a function of the top gate was observed. After the inflection point, the induced built-in electric field was saturated and not enough to continue canceling the applied top gate voltage. The top gate thus regained its tunability. A reverse process is also

applicable to the backward scanning of top gate sweeping, indicated by the blue color of the negative differential resistance peak in Figure 3a.

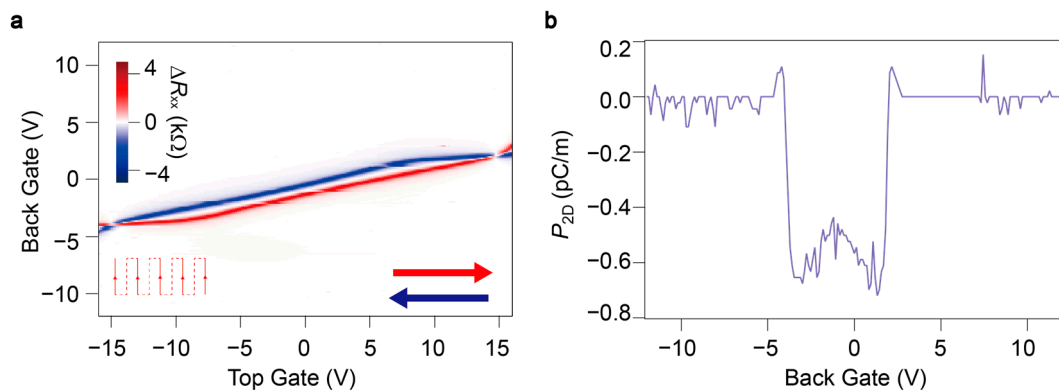


Figure 3. Hysteretic transport behavior and polarization. (a) The difference ΔR_{xx} between the measured resistance values in Figure 2a,b. The red line represents the resistance peak line when the V_{TG} scans upwards from -15 V to 15 V, while the blue line represents the resistance peak with a downward scanning direction. All the data adopted the resistance when the back gate was scanned upwards from -12 V to 12 V. (b) The estimated induced polarization P_{2D} at different V_{BG} by using the formula $P_{2D} = e\Delta n_P d_T$, where the P_{2D} represents the two-dimensional polarization, e represents the electron charge, Δn_P represents half of the carrier density difference between the upwards and downwards scan direction of V_{TG} , and d_T represents the distance between the top h-BN and the twisted graphene.

For typical dual-gated graphene without extra interface ferroelectric polarization, the resistance peak corresponds to the charge neutrality usually followed by a straight diagonal line (the charge neutral line, where $n = 0$), which would have no hysteresis for forwards and downwards gate sweeping directions. As for our twisted graphene device, a shift of charge neutrality occurred in the form of hysteresis as the top gate is scanned back and forth, exhibiting an extra charge Δn_P induced by the interface-ferroelectric polarization. The induced polarization P_{2D} can thus be estimated at every V_{BG} by using the formula $P_{2D} = e\Delta n_P d_{TG}$, where e represents the electron charge, and d_{TG} represents the distance between the top h-BN and the TBLG. Here the $2\Delta n_P$ was estimated by using Gauss's law $2\Delta n_P = \epsilon_{BN}\Delta V_{TG}/d_T$. Our top dielectric layer consists of h-BN and AlO_x in serial with similar dielectric constants of $4\epsilon_0$, where ϵ_0 is the vacuum dielectric constant. The estimated P_{2D} at different back gate voltage was shown in Figure 3b, with a maximum P_{2D} of about 0.7 pC/m. The estimated polarization is found to be in the same order of magnitude as reported for other 2D sliding ferroelectric systems [16–20]. From Figure 3b, we can also see that P_{2D} seemed to be a constant, regardless of the value of V_{BG} when the interface was ferroelectrically polarized.

4. Conclusions

We have fabricated a high-quality h-BN-encapsulated 30° -twisted bilayer-graphene device. A robust 2D ferroelectric polarization was evidenced at the top interface. The 2D ferroelectric polarization leads to a built-in electrical field at the top interface, which yields a tunable hysteretic behavior in the field effect curve as a function of the top gate from room temperature down to 4 mK. According to the well-established GFSE model, the interface-ferroelectric polarization was estimated to be 0.7 pC/m in our system. Our findings may help to expand the 2D sliding ferroelectricity to a broader family of heterostructures. In the meantime, the combination between TBLG and ferroelectric polarization may be a platform for future investigations of multiple quantum degrees of freedom in complex devices.

Supplementary Materials: The following supporting information can be downloaded at: <https://www.mdpi.com/article/10.3390/magnetochemistry9050116/s1>, Figure S1: Optical images of the several steps of the fabrication process of sample S1; Figure S2: Optical images of samples with the same structure that we fabricated. S1 is the sample mentioned in the main text with ferroelectric polarization, while S2–S7 are samples without ferroelectricity; Figure S3: Dual gate mapping of the samples S2–S7 at 40 mK.

Author Contributions: Conceptualization, methodology, formal analysis, L.R. and B.D.; sample fabrication, L.R.; data curation, L.R. and B.D.; discussion, L.R. and B.D.; writing—original draft preparation, L.R.; writing—review and editing, B.D. All authors have read and agreed to the published version of the manuscript.

Funding: This work was supported by the National Natural Science Foundation of China (NSFC) (Grant Nos. 12004228 and U21A6004).

Institutional Review Board Statement: Not applicable.

Informed Consent Statement: Not applicable.

Data Availability Statement: All data associated with this manuscript is published in the text.

Acknowledgments: We thank Zheng Han for providing fruitful discussion and modifying the manuscript.

Conflicts of Interest: The authors declare no conflict of interest.

References

1. Martin, L.W.; Rappe, A.M. Thin-film ferroelectric materials and their applications. *Nat. Rev. Mater.* **2016**, *2*, 16087. [[CrossRef](#)]
2. Bertolazzi, S.; Bondavalli, P.; Roche, S.; San, T.; Choi, S.Y.; Colombo, L.; Bonaccorso, F.; Samori, P. Nonvolatile memories based on graphene and related 2D materials. *Adv. Mater.* **2019**, *31*, 1806663. [[CrossRef](#)] [[PubMed](#)]
3. Khan, A.I.; Keshavarzi, A.; Datta, S. The future of ferroelectric field effect transistor technology. *Nat. Electron.* **2020**, *3*, 588–597. [[CrossRef](#)]
4. Wang, X.; Yasuda, K.; Zhang, Y.; Liu, S.; Watanabe, K.; Taniguchi, T.; Hone, J.; Fu, L.; Jarillo-Herrero, P. Interfacial ferroelectricity in rhombohedral-stacked bilayer transition metal dichalcogenides. *Nat. Nanotechnol.* **2022**, *17*, 367–371. [[CrossRef](#)] [[PubMed](#)]
5. Wu, M.; Li, J. Sliding ferroelectricity in 2D van der Waals materials: Related physics and future opportunities. *Proc. Natl. Acad. Sci. USA* **2021**, *118*, e2115703118. [[CrossRef](#)]
6. Zhou, Y.; Wu, D.; Zhu, Y.; Cho, Y.; He, Q.; Yang, X.; Herrera, K.; Chu, Z.; Han, Y.; Downer, M.C.; et al. Out-of-Plane Piezoelectricity and Ferroelectricity in Layered α -In₂Se₃ Nanoflakes. *Nano Lett.* **2017**, *17*, 5508–5513. [[CrossRef](#)]
7. Cui, C.; Hu, W.J.; Yan, X.; Addiego, C.; Gao, W.; Wang, Y.; Wang, Z.; Li, L.; Cheng, Y.; Li, P.; et al. Intercorrelated In-Plane and Out-of-Plane Ferroelectricity in Ultrathin Two-Dimensional Layered Semiconductor In₂Se₃. *Nano Lett.* **2018**, *18*, 1253–1258. [[CrossRef](#)]
8. Liu, F.; You, L.; Seyler, K.L.; Li, X.; Yu, P.; Lin, J.; Wang, X.; Zhou, J.; Wang, H.; He, H.; et al. Room-temperature ferroelectricity in CuInP₂S₆ ultrathin flakes. *Nat. Commun.* **2016**, *7*, 12357. [[CrossRef](#)]
9. Belianinov, A.; He, Q.; Dziazugys, A.; Maksymovych, P.; Eliseev, E.; Borisevich, A.; Morozovska, A.; Banys, J.; Vysochanskii, Y.; Kalinin, S.V. CuInP₂S₆ Room Temperature Layered Ferroelectric. *Nano Lett.* **2015**, *15*, 3808–3814. [[CrossRef](#)]
10. Jiang, X.; Wang, X.; Wang, X.; Zhang, X.; Niu, R.; Deng, J.; Xu, S.; Lun, Y.; Liu, Y.; Xia, T.; et al. Manipulation of current rectification in van der Waals ferroionic CuInP₂S₆. *Nat. Commun.* **2022**, *13*, 574. [[CrossRef](#)]
11. Chang, K.; Liu, J.; Lin, H.; Wang, N.; Zhao, K.; Zhang, A.; Jin, F.; Zhong, Y.; Hu, X.; Duan, W.; et al. Discovery of robust in-plane ferroelectricity in atomic-thick SnTe. *Science* **2016**, *353*, 274–278. [[CrossRef](#)]
12. Zheng, C.; Yu, L.; Zhu, L.; Collins, J.L.; Kim, D.; Lou, Y.; Xu, C.; Li, M.; Wei, Z.; Zhang, Y.; et al. Room temperature in-plane ferroelectricity in van der Waals In₂Se₃. *Sci. Adv.* **2018**, *4*, eaar7720. [[CrossRef](#)]
13. Higashitarumizu, N.; Kawamoto, H.; Lee, C.J.; Lin, B.H.; Chu, F.H.; Yonemori, I.; Nishimura, T.; Wakabayashi, K.; Chang, W.H.; Nagashio, K. Purely in-plane ferroelectricity in monolayer SnS at room temperature. *Nat. Commun.* **2020**, *11*, 2428. [[CrossRef](#)]
14. Wang, Y.; Li, W.; Guo, Y.; Huang, X.; Luo, Z.; Wu, S.; Wang, H.; Chen, J.; Li, X.; Zhan, X.; et al. A gate-tunable artificial synapse based on vertically assembled van der Waals ferroelectric heterojunction. *J. Mater. Sci. Technol.* **2022**, *128*, 239–244. [[CrossRef](#)]
15. Li, W.; Guo, Y.; Luo, Z.; Wu, S.; Han, B.; Hu, W.; You, L.; Watanabe, K.; Taniguchi, T.; Alava, T.; et al. A Gate Programmable van der Waals Metal-Ferroelectric-Semiconductor Vertical Heterojunction Memory. *Adv. Mater.* **2022**, *35*, 2208266. [[CrossRef](#)]
16. Zheng, Z.; Ma, Q.; Bi, Z.; de La Barrera, S.; Liu, M.H.; Mao, N.; Zhang, Y.; Kiper, N.; Watanabe, K.; Taniguchi, T.; et al. Unconventional ferroelectricity in moiré heterostructures. *Nature* **2020**, *588*, 71–76. [[CrossRef](#)]
17. Yasuda, K.; Wang, X.; Watanabe, K.; Taniguchi, T.; Jarillo-Herrero, P. Stacking-engineered ferroelectricity in bilayer boron nitride. *Science* **2021**, *372*, 1458–1462. [[CrossRef](#)]

18. Vizner, S.M.; Waschitz, Y.; Cao, W.; Nevo, I.; Watanabe, K.; Taniguchi, T.; Sela, E.; Urbakh, M.; Hod, O.; Ben Shalom, M. Interfacial ferroelectricity by van der Waals sliding. *Science* **2021**, *372*, 1462–1466. [[CrossRef](#)]
19. Woods, C.R.; Ares, P.; Nevison-Andrews, H.; Holwill, M.J.; Fabregas, R.; Guinea, F.; Geim, A.K.; Novoselov, K.S.; Walet, N.R.; Fumagalli, L. Charge-polarized interfacial superlattices in marginally twisted hexagonal boron nitride. *Nat. Commun.* **2021**, *12*, 347. [[CrossRef](#)]
20. Niu, R.; Li, Z.; Han, X.; Qu, Z.; Ding, D.; Wang, Z.; Liu, Q.; Liu, T.; Han, C.; Watanabe, K.; et al. Giant ferroelectric polarization in a bilayer graphene heterostructure. *Nat. Commun.* **2022**, *13*, 6241. [[CrossRef](#)]
21. Shen, C.; Chu, Y.; Wu, Q.; Li, N.; Wang, S.; Zhao, Y.; Tang, J.; Liu, J.; Tian, J.; Watanabe, K.; et al. Correlated states in twisted double bilayer graphene. *Nat. Phys.* **2020**, *16*, 520–525. [[CrossRef](#)]
22. Park, J.M.; Cao, Y.; Watanabe, K.; Taniguchi, T.; Jarillo-Herrero, P. Tunable strongly coupled superconductivity in magic-angle twisted trilayer graphene. *Nature* **2021**, *590*, 249–255. [[CrossRef](#)] [[PubMed](#)]
23. Cao, Y.; Rodan-Legrain, D.; Rubies-Bigorda, O.; Park, J.M.; Watanabe, K.; Taniguchi, T.; Jarillo-Herrero, P. Tunable correlated states and spin-polarized phases in twisted bilayer–bilayer graphene. *Nature* **2020**, *583*, 215–220. [[CrossRef](#)]
24. Liu, X.; Hao, Z.; Khalaf, E.; Lee, J.Y.; Ronen, Y.; Yoo, H.; Haei Najafabadi, D.; Watanabe, K.; Taniguchi, T.; Vishwanath, A.; et al. Tunable spin-polarized correlated states in twisted double bilayer graphene. *Nature* **2020**, *583*, 221–225. [[CrossRef](#)] [[PubMed](#)]
25. Arora, H.S.; Polski, R.; Zhang, Y.; Thomson, A.; Choi, Y.; Kim, H.; Lin, Z.; Wilson, I.Z.; Xu, X.; Chu, J.H.; et al. Superconductivity in metallic twisted bilayer graphene stabilized by WSe₂. *Nature* **2020**, *583*, 379–384. [[CrossRef](#)]
26. Klein, D.R.; Xia, L.Q.; MacNeill, D.; Watanabe, K.; Taniguchi, T.; Jarillo-Herrero, P. Electrical switching of a bistable moiré superconductor. *Nat. Nanotechnol.* **2023**, *30*, 331–335. [[CrossRef](#)]
27. Yao, W.; Wang, E.; Bao, C.; Zhang, Y.; Zhang, K.; Bao, K.; Chan, C.K.; Chen, C.; Avila, J.; Asensio, M.C.; et al. Quasicrystalline 30 twisted bilayer graphene as an incommensurate superlattice with strong interlayer coupling. *Proc. Natl. Acad. Sci. USA* **2018**, *115*, 6928–6933. [[CrossRef](#)]
28. Sanchez-Yamagishi, J.D.; Taychatanapat, T.; Watanabe, K.; Taniguchi, T.; Yacoby, A.; Jarillo-Herrero, P. Quantum Hall effect, screening, and layer-polarized insulating states in twisted bilayer graphene. *Phys. Rev. Lett.* **2012**, *108*, 076601. [[CrossRef](#)]
29. Ahn, S.J.; Moon, P.; Kim, T.H.; Kim, H.W.; Shin, H.C.; Kim, E.H.; Cha, H.W.; Kahng, S.J.; Kim, P.; Koshino, M.; et al. Dirac electrons in a dodecagonal graphene quasicrystal. *Science* **2018**, *361*, 782–786. [[CrossRef](#)]
30. Spurrier, S.; Cooper, N.R. Theory of quantum oscillations in quasicrystals: Quantizing spiral Fermi surfaces. *Phys. Rev. B* **2019**, *100*, 081405. [[CrossRef](#)]
31. Sun, X.; Zhang, S.; Liu, Z.; Zhu, H.; Huang, J.; Yuan, K.; Wang, Z.; Watanabe, K.; Taniguchi, T.; Li, X.; et al. Correlated states in doubly-aligned hBN/graphene/hBN heterostructures. *Nat. Commun.* **2021**, *12*, 7196. [[CrossRef](#)] [[PubMed](#)]
32. Wang, Y.; Gao, X.; Yang, K.; Gu, P.; Lu, X.; Zhang, S.; Gao, Y.; Ren, N.; Dong, B.; Jiang, Y.; et al. Quantum Hall phase in graphene engineered by interfacial charge coupling. *Nat. Nanotechnol.* **2022**, *17*, 1272–1279. [[CrossRef](#)] [[PubMed](#)]
33. Saito, Y.; Ge, J.; Watanabe, K.; Taniguchi, T.; Young, A.F. Independent superconductors and correlated insulators in twisted bilayer graphene. *Nat. Phys.* **2020**, *16*, 926–930. [[CrossRef](#)]
34. Lin, J.X.; Zhang, Y.H.; Morissette, E.; Wang, Z.; Liu, S.; Rhodes, D.; Watanabe, K.; Taniguchi, T.; Hone, J.; Li, J.I. Spin-orbit–driven ferromagnetism at half moiré filling in magic-angle twisted bilayer graphene. *Science* **2022**, *375*, 437–441. [[CrossRef](#)]

Disclaimer/Publisher’s Note: The statements, opinions and data contained in all publications are solely those of the individual author(s) and contributor(s) and not of MDPI and/or the editor(s). MDPI and/or the editor(s) disclaim responsibility for any injury to people or property resulting from any ideas, methods, instructions or products referred to in the content.